

Activation-Induced Surface Modulation of Biowaste-Derived Hierarchical Porous Carbon for Supercapacitors

Pratigya Sharma,^[a] Deobrat Singh,^[b] Manickam Minakshi,*^[a] Saleha Quadsia,^[a] and Rajeev Ahuja^[b, c]

Wheat straw-derived carbon from the Wheatbelt region in Western Australia was subjected to chemical activation in an electrolyte containing either acid or base treatment. The findings showed an increase in electron/hole mobility towards the interfaces due to the presence of different surface functional groups such as C–SO_x–C and S=C in the carbon framework for acid activation. Likewise, the galvanostatic capacitance measured at a current density of 2 mA cm^{−2} in a three-electrode

configuration for acid-activated wheat straw exhibited 162 F g^{−1}, while that for base-activated wheat straw exhibited 106 F g^{−1}. An increase of 34.5% more capacitance was achieved for acid-treated wheat straw. This improvement is attributed to the synergistic effects between surface functional groups and electrolyte ions, as well as the electronic structure of the porous electrode.

Introduction

The rapid consumption of finite fossil fuels with the resultant environmental pollution has been intimately linked to global warming and is considered a primary factor in climate change. A sustainable roadmap toward harnessing renewable energy is of utmost importance to negate the environmental effect caused by the excessive use of fossil fuels.^[1] Developing sustainable electrodes for energy storage applications is intensely researched to address the intermittent nature of renewable energy. The electrodes in the energy storage system (fuel cells, batteries, supercapacitors) capture the energy produced from renewable sources and convert it to economically storable forms. The efficiency of these storage technologies is quantified based on the parameters of storage capacity, energy and power density, and longevity of the system which entirely depends on the chosen electrode material.^[2] Supercapacitors have electrochemical properties that complement the characteristics of the battery and emerged as promising

alternatives. Some of the end-uses for supercapacitors include airborne wind and solar capacity firming, heavy-duty vehicles, hybrid-electric transit buses, etc. Aqueous supercapacitors using an aqueous NaOH electrolyte could find a major application in the stationary energy storage field, where the cost and safety of water-based systems play a crucial role. Moreover, it is recognized that biomass-derived activated carbon electrode materials are cost-effective with energy storage capability primarily originating from reversible faradaic reactions that emanate from the high surface area of the carbon electrode. The activated carbon also possesses a high specific surface area and a large volume of micropores, high electrical conductivity, tunable morphology and porosity, excellent mechanical strength and good stability, and compatibility in a composite material, making it an attractive material.^[3] The traditional source of activated carbon (AC) has been petroleum coke and feeds, pitches which are non-renewable sources involving mining and environmental hazard. However, making AC from renewable sources is more valid because it is sustainable. The carbonization of abundant and diversified bioresources has been studied widely as precursors for the preparation of activated carbon. Hierarchical porous carbon materials derived from biomass, which is a rich source of carbon, with interconnected pores, offer excellent properties including a high surface area and abundant reaction sites for surface functional groups to interact and be suitable for potential applications such as energy storage.

The diversity in biomass composition and activation processes hugely affects the performance of biomass-derived carbon for energy storage applications.^[4] Optimising the structure and pore size distribution remains unique to the chosen biomass precursors, method of preparation, and the elemental ratios present in them. The key to unlocking the potential for new electrode designs resides in the surface modulation accompanying the high-performance energy storage properties. Several approaches have been employed to modulate the electronic properties of carbon materials via

[a] P. Sharma, Dr. M. Minakshi, S. Quadsia
College of Science, Health, Engineering and Education
Murdoch University
Perth WA 6150 (Australia)
E-mail: minakshi@murdoch.edu.au

[b] Dr. D. Singh, Prof. R. Ahuja
Condensed Matter Theory Group, Materials Theory Division, Department of
Physics and Astronomy
Uppsala University
Box 516, 75120, Uppsala (Sweden)

[c] Prof. R. Ahuja
Department of Physics
Indian Institute of Technology Ropar
Rupnagar 140001, Punjab (India)

Supporting information for this article is available on the WWW under
<https://doi.org/10.1002/cplu.202200126>

© 2022 The Authors. ChemPlusChem published by Wiley-VCH GmbH. This is an open access article under the terms of the Creative Commons Attribution Non-Commercial License, which permits use, distribution and reproduction in any medium, provided the original work is properly cited and is not used for commercial purposes.

surface transfer doping, substitutional doping, electrostatic gating, and the introduction of atomic defects.^[4–7] Similar to semiconductor doping, doping of heteroatoms such as boron (B), nitrogen (N), and sulfur (S) into the carbon lattice is a standard exercise practiced to modulate their electronic properties.^[8–12] The introduction of various atoms to carbon structure is widely studied for various applications.^[3,13–16] Hence, in this work, an attempt to achieve the surface modulation on activated carbon has been carried out through different chemical activation processes using acid and base reagents and identified their structural, electronic, and electrochemical properties. A comparative table showing the use of different biomass sources, activating agent and its performance is tabulated in Table S1. The uniqueness of the biomass employed in this study has been detailed below.

The wheat industry of WA (Western Australia) accounts for 65% of the grain production covering 1000–1500 hectares of land and contributes ~A\$ 2–3 billion for the state economy annually (Department of Primary Industries and Regional Development, 2019).^[17] About 7 million tonnes of wheat straw also termed “cereal straw”, obtained as a by-product after harvesting of wheat, are produced every year which significantly contributes to biomass waste. This agricultural waste is lignocellulosic biomass composed mainly of cellulose, hemicellulose, and smaller content of lignin.^[18] From region to region, these components vary owing to their structural and functional complexity. The biomass contains an average calorific value of 15 MJ/Kg with a lower heating value of 29 MJ/Kg. Wheat straw has been widely employed as an inexpensive resource to produce bioethanol and biogas in biorefineries industries. In our region in WA, the cereal straw has been employed to co-fire with coal in the Collie power station. This is one of the major electricity generating coal-fired power stations in WA, which uses coal from Collie coal fields as its primary energy source. The prevalence of cereal straw in Collie with functional ingredients and bioactive moieties has led to thinking as to whether this biomass could form the basis of inexpensive carbon precursor. If this biomass is viable, it not only reduces the emissions associated with the burning (co-firing) of the straws but also the cellulose structure makes it more suitable by the formation of hydrogen bonding during the hydrolysis.^[19]

The overall aim of the current study is to highlight the repurposing of the cereal straw from the WA region as a novel carbon electrode. The novelty of the study is the application of cereal straw obtained from our regional area having a rich content of carbon (tabulated in Table 1) along with other functional elements H, N, O, and S through chemical activation processing.^[20,21] Here, a novel carbon electrode derived from wheat straw from the Wheatbelt region of WA was employed as a biomass precursor and found to be suitable for aqueous-based supercapacitor. It is demonstrated that wheat straw-derived activated carbon from H₂SO₄ as an activating agent exhibits excellent supercapacitance properties due to well-defined porous and surface functional features originating from this region than the traditionally used KOH activating agent. A

Table 1. Elemental analysis of raw wheat straw from WA, compared its proportion after activation and carbonization processes, WS-acid and WS-base.

Sample – Untreated raw wheat straw Proximate analysis [wt.%]		Content of inorganic elements			
Moisture	7.0	Na	0.2	Al	0.4
Volatile matter	75.8	K	15.8	Na	0.2
Fixed carbon	7.3	Mg	0.9	P	0.2
Ash	16.9	Ca	0.9	Si	12.5

Ultimate analysis of wheat straw [wt %]			
Element	Untreated raw wheat straw	WS-acid	WS-base
C	46.3	79.12	84.02
H	5.5	0.8	0.9
N	0.2	1.78	1.63
S	0.06	0.18	0.08
O	47.5	18.12	13.4

comparison of these activating agents has been shown in detail.

Therefore, this study provides the first of its kind assessing the fabrication of highly capacitive AC using a bio-waste wheat straw involving H₂SO₄ as an activating agent with the energetics determined by density functional theory calculations support our attribution of the formation of different atoms on the C structure.

Results and Discussion

Physical and chemical properties

Hierarchical porous carbon meso- and micropores were obtained following the chemical activation method. Our study offer evidence that diversity in the chemical composition of the chosen biomass precursor and activation process affects both the physical properties and electrochemical supercapacitive performance.

Proximate analysis, a basic yet important analysis, was carried out to determine moisture content, volatile matter (VM), fixed carbon (FC), and ash of the untreated biomass precursor wheat straw (WS). After this, ultimate elemental analysis of the untreated WS was compared with the final products, i.e., WS-acid and WS-base, to determine the changes in the elemental composition of carbon, hydrogen, nitrogen, oxygen, and sulfur. In addition, the content of inorganic elements (that do not contain carbon) present was evaluated for the untreated WS as it could significantly affect various physical and electrochemical properties. Obtained result of the proximate and ultimate analysis is presented in Table 1. It shows considerable changes in elemental composition because of the treatment and its activating agents. After carbonization, the volatile content in the precursor decreased, especially in the base treatment.

The two-step synthesis processes of biomass-derived carbon are schematically illustrated in Figure 1. The process of converting WS precursors into their derived AC primarily involves two

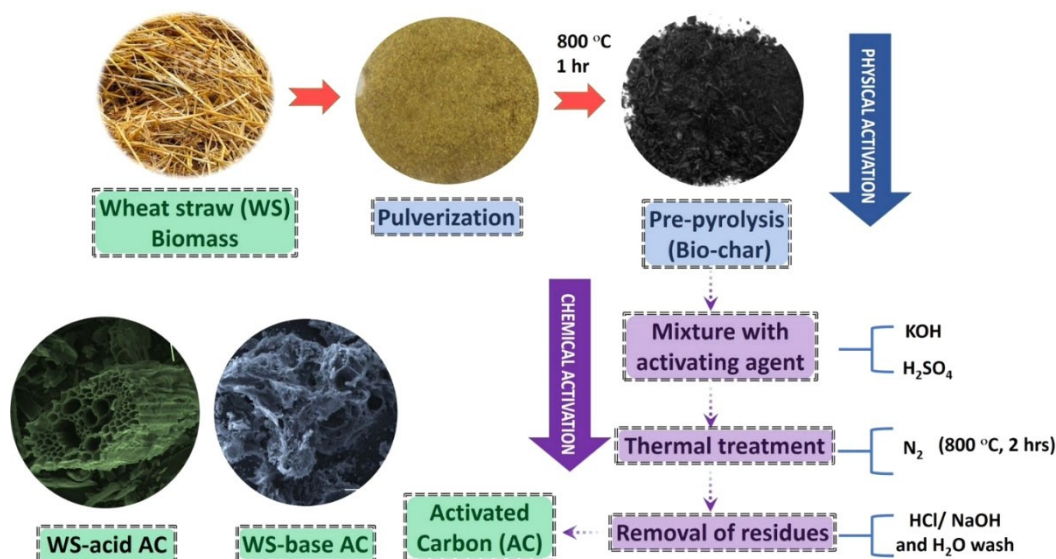


Figure 1. Schematic representation illustrating steps involved in preparing biomass-derived activated carbon from wheat straw (WS).

steps, which are pyrolysis and activation. The role of pyrolysis is to decompose the WS at elevated temperature in the Ar atmosphere while the subsequent step activation involves both physical and chemical to achieve the goal of obtaining a hierarchical porous network. The first step is to enhance the surface area and porosity whereas the activation process accommodates a range of porosity like meso- and micropore, which are pre-requisites for any electrodes for supercapacitor applications. A noticeable difference in the morphologies of synthesized AC was confirmed by field emission scanning electron microscope (FE-SEM) images of the WS-acid and WS-base derived products (Figure 2). The image of acid pre-treated WS shows a microtubular hierarchical porous structure, whereas the base pre-treated WS does not have any defined morphology but a disordered porous structure on the surface, which accounts for the attack of KOH. The magnified image of the WS acid exhibited a hierarchical porous network comprising both macro-structures along with meso- and micropores with carbon layers. The observed changes (between Figure 2 C and F) can be attributed to the chemical activation process of the raw biomass that changes the polarity and acidity of the carbon surface. TEM images of WS-acid, which performed better (explained in section 2.2.) than WS-base in terms of its capacitance, are presented in Figure 2 G and H. The TEM image shows the presence of a few graphite sheets on the edges of the bulk structure. This is in excellent agreement with the microporous structure and the presence of the carbon layer observed through SEM images. The elemental mapping (in Figure 2 I–L) ascertains the presence of desired elements, i.e., C, N, and O, along with some traces of Si which was present in the raw WS. This observation is also in accordance with the proximate elemental analysis presented in Table 1. The results are particularly remarkable because the introduction of a desired functional group/atoms with various macro-structural morphology is achieved when the same WS is pre-treated and

activated with a different activating agent, which is not well-known for acid reagents. Our approach of using a new WS biomass with an H₂SO₄ activating agent, therefore, offers an alternative to the porous network currently observed for KOH activating agents. Such large hierarchical porous graphitic carbon through the nature of activating agent is unprecedented. A plausible mechanism that could bring out the variation in the observed morphologies is demonstrated here.

KOH activation aids in generating porous carbon structure as it etches the carbon frame via a redox reaction generated by potassium-based compounds (K₂CO₃, K₂O) from the activating agent. The metallic K involved during the activation process intercalates with the carbon lattices resulting in its expansion. This metallic K and K-based compound can be removed by repeated washing in the later stage. The carbon lattices cannot revert to their original position after removing these intermediate products, leading to porous structure formation.^[22,23] Whereas, acids such as H₂SO₄ and HNO₃ generally act as oxidizing and a dehydrating agents. Moreover, the presence of silicon as inorganic compounds in the untreated biomass precursor can lead to catalytic graphitization. During the activation process, the presence of abundant surface oxygen functional groups (C=O, O–C=O, –OH, –SOx, etc) favour the dispersion of Si to obtain high carbon yield. In such a process, a dissolution-precipitation mechanism occurs where the metal nanoparticles diffuse through the amorphous carbon leaving behind a network of hierarchical porous graphitic carbon.^[24,25] Hence, the presence of Si facilitates high-yield porous carbon structure.

To further confirm the presence of graphitic carbon of as-synthesized AC, X-ray diffraction (XRD) was employed. XRD patterns of the WS-acid and WS-base derived ACs (in Figure 3 A) reflect relatively well-defined two peaks located at 22° and 43° representing the characteristic graphitic carbon reflections with an increased order of carbon corresponding to (002) and (101). A slightly weak intensity peak of WS-acid implies the

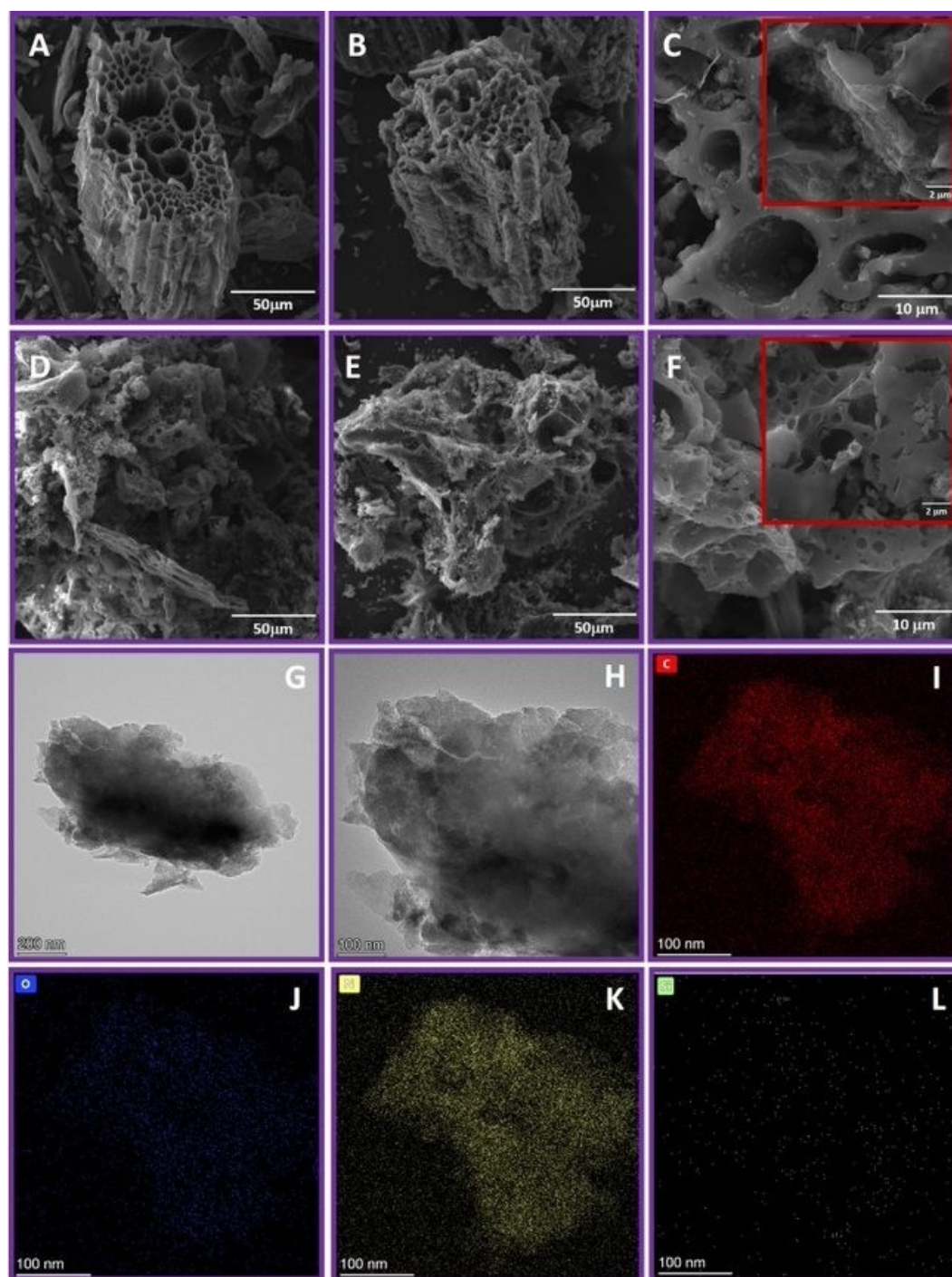


Figure 2. FE-SEM images of (A to C) WS-acid, and (D to F) WS-base with different magnification. The insets in C and F show highly magnified images of WS-acid and WS-base, respectively. (G and H) TEM images of WS-acid with different magnification, and (I to L) elemental mapping demonstrating the elements present in WS-acid.

amorphous carbon having more defect formation otherwise lateral disordering because of the chosen activating agent, in addition to the contribution coming from the impurities present in the raw wheat straw. These results confirm the successful formation of as-synthesized AC. The thermogravimetric analysis (TGA) as shown in Figure 3 B aided in calculating the information on the sample's proximate analysis as presented in

Table 1. In addition, information on the thermal stability of the material and appropriate temperature for degassing the sample for surface area analysis can also be studied simultaneously. The TGA profile revealed a weight loss at 70 to 150 °C, which corresponds to the desorption of physisorbed water, and another significant weight loss at 250 to 500 °C which implies carbon pyrolysis. To gain some insights into the degree of

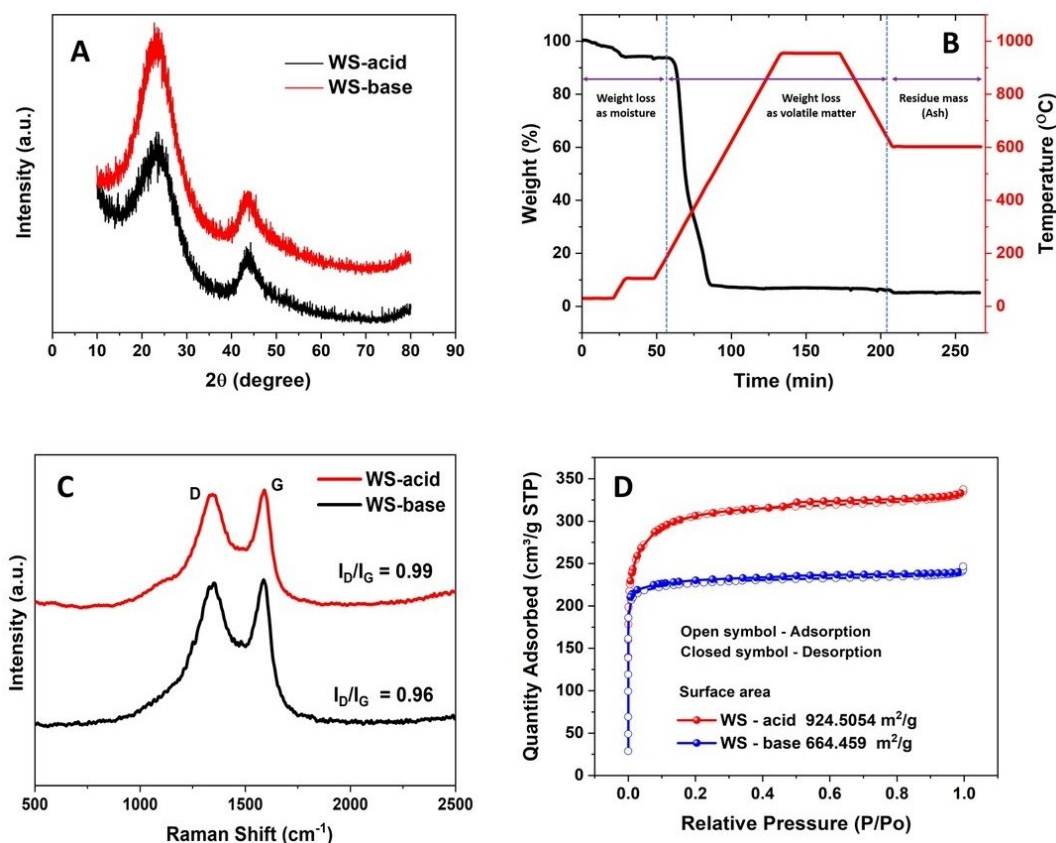


Figure 3. (A) X-ray diffraction (XRD) pattern of WS-acid and WS-base, (B) Thermo-gravimetric analysis (TGA) of raw biomass, (C) Raman spectrum of WS-acid and WS-base showing D and G band, (D) Brunauer-Emmett-Teller (BET) nitrogen adsorption hysteresis loops of WS-acid and WS-base as indicated in the figure.

ordering in a carbon sample, the Raman spectra of WS-acid and WS-base derived ACs were analyzed, and the results are shown in Figure 3 C. Two typical characteristic peaks for AC, i.e., D and G band, were observed at $\sim 1340\text{ cm}^{-1}$ and 1580 cm^{-1} , respectively. The D band represents the structural defect corresponding to sp^3 hybridized carbon atoms in the structure, whereas the G band is the in-plane vibration of sp^2 hybridized carbon atoms relating to the graphitic order.^[26] A defect-free carbon lacks a D peak. The intensity ratio of the D band (I_D) to G band (I_G) gives information on graphitic clusters present in the disordered carbon and the extent of graphitization.^[27] As shown in Figure 3 C, the I_D/I_G value of WS-acid and WS-base were 0.99 and 0.96, respectively. This implies that more defect sites were introduced via the acid activation process. In this scenario, activation-induced surface modulation is ascertained due to the nature of the functional group present in the carbon structure and the elemental composition of the material.

To examine the textual properties of ACs, the Brunauer-Emmett-Teller (BET) specific surface area of WS-acid and WS-base were performed. The resulting isotherm in Figure 3 D exhibits a hysteresis loop with a type IV that is typical for mesoporous material.^[28] The BET surface area of WS-acid is $924\text{ m}^2\text{ g}^{-1}$, while the surface area of WS-base is $664\text{ m}^2\text{ g}^{-1}$. This variation in surface area is presumably due to the different activating agents. The higher surface area of WS-acid associated

with mesopores will be critically important in the superior electrochemical performance such as sufficient charge storage along with the rate capability with enhanced charge transfer kinetics. The pore size distribution profile is given in Figure S1.

Surface functional groups of the WS-acid and WS-base-derived ACs were analyzed by Fourier transform infrared spectroscopy (FTIR). The observed spectral differences of the samples imply that the activation process using different agents has led to significant changes in the chemical composition. FTIR spectra of WS- raw precursor (inactivated) are compared with WS-acid and WS-base in Figure S2. Cellulose, starch, and lignin are the chief component present in any typical biomass. In our pristine sample, WS-raw shows the presence of various functional groups such as hydroxyl, carbonyl carboxyl, ketonic as common functional groups present in a lignocellulose material. The decrease in absorption at $\sim 572\text{ cm}^{-1}$ (Si–O) for treated WS signifies the partial removal of ash.^[29] The peaks in the region 1000 to 1400 cm^{-1} denote the presence of C–O, and C–H groups. For the activation-induced samples, the significant decrease in the peak intensity at $\sim 1025\text{ cm}^{-1}$ corresponding to C–O–C stretching polysaccharides suggests depletion of cellulose components. The broader peak positioned at $\sim 1309\text{ cm}^{-1}$ corresponds to CH and C–O stretching of guaiacyl lignin.^[30] The band positioned at $\sim 1568\text{ cm}^{-1}$ represents the aromatic ring C=C stretching in lignin. Further, the IR peak at the 2300 to

2700 cm^{-1} region attributed to the C–H (CH_3 and CH_2) stretching vibration of polysaccharides/lignin.^[30] The band observed at $\sim 3349 \text{ cm}^{-1}$ is related to hydrogen-bonded (O–H) stretching in methyl groups of lignin and water in the raw biomass.^[31] For both the WS-acid and WS-base derived ACs, the intensities of the band related to the C–O–C group that corresponds to cellulose and hemicellulose decreased and becomes less prominent. This could be because of carbonization. Also, the elements O and H are removed considerably for the carbonized samples as the volatile substances are easily removed during the thermal treatment. The remaining results in carbon form as graphitic, turbostratic, or hybrid form.^[32]

To gain information on surface of biomass samples, X-ray photoelectron spectroscopy (XPS), a surface-sensitive technique is carried out. Figure S3 depicts the wide XPS spectra of the samples having major components of C, N, O and a minor peak for S. For the WS-acid and WS-base derived ACs, we can observe carbon atoms and other heteroatoms, mainly O and N distributed on the surface, which is a typical feature possessed by carbon derived from biomass material (Figure 4).^[33] Detailed analysis of core-level spectra for various elements reveals that the change in surface composition occurs for the WS-acid and WS-base derived ACs. Four well-resolved peaks at 284.6 eV, 531 eV, 400 eV, and 164 eV are observed (Figure 4A–D) for WS-acid corresponding to C 1s, O 1s, N 1s, and S 2p. While three well-resolved peaks C 1s, O 1s, and N 1s could be observed for

WS-base. The presence of S 2p in Figure 4D comes from the WS-acid (H_2SO_4) activating agent. The high-resolution XPS spectra for C 1s are fitted with three other sub-peaks. The major peak at 284.6 eV representing sp^2 carbons suggests that most of the C in the WS-acid sample is graphitic. Two other peaks at 285.91 eV and 289.50 eV are fitted to –C–OH and –CO groups.^[34] In the case of WS-base, KOH enabled activation, (Figure 4E), the presence of K 2p is seen, which could be a result of K atom diffusion in the C framework. Even after repeated washing with a copious number of solvents, some residues could have remained in the WS-base sample, as evidenced by the XPS K 2p spectra. Similarly, both WS-acid and WS-base showed the presence of heteroatoms. The O 1s spectra possessed three well-fitted peaks of oxygen-containing functional groups C–O, C=O, and O–C=O between 531 eV to 533 eV corresponding to carbonyl and C–OH groups as shown in Figures 4B and 4F.^[35] The fitted nitrogen spectra (Figure 4C and G) show the clear presence of pyrrolic and pyridinic peaks at $\sim 401 \text{ eV}$ and 398 eV .^[36] In addition to the above-mentioned spectra, in the case of WS-acid, the S 2p spectrum (Figure 4D) with subpeaks at 164 eV and 168 eV relating to S=C and C– SO_x –C respectively can be observed, which can be attributed to the H_2SO_4 as activation agent.^[27] This result indicates that activation-induced changes in the surface's properties are due to the chemical composition resulting from different activation agents such as KOH and H_2SO_4 .

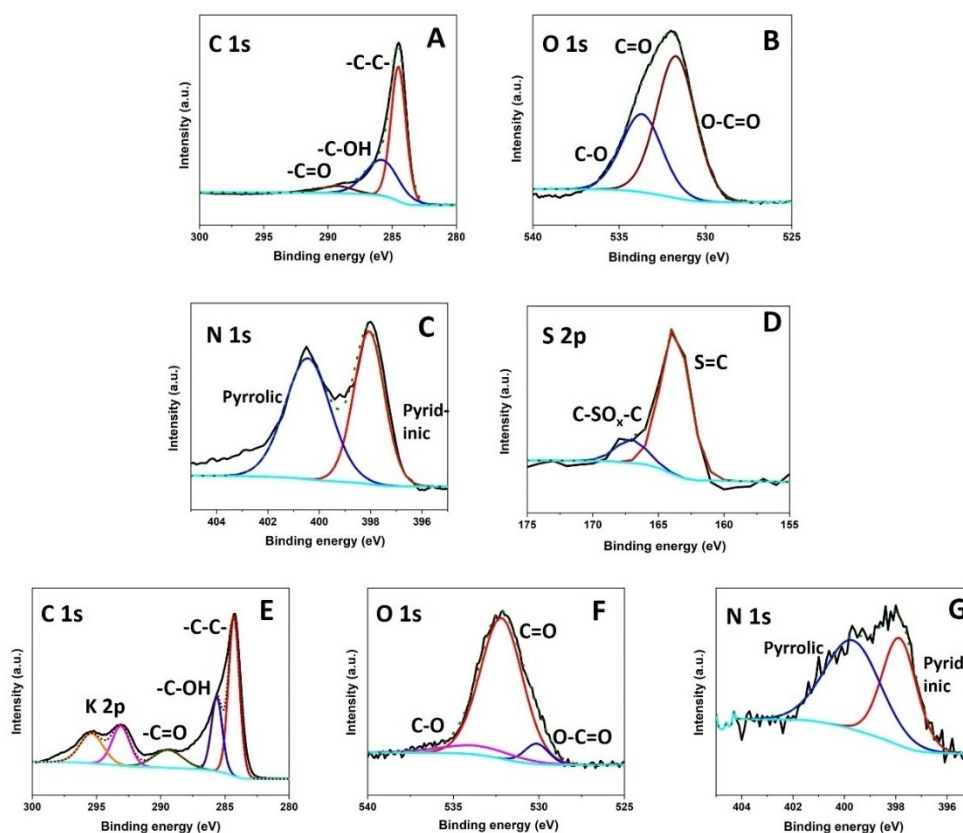


Figure 4. High-resolution fitted X-ray photoelectron spectroscopy (XPS) spectra of (A to D) C 1s, O 1s, N 1s, and S 2p of WS acid and (E to G) C 1s, O 1s, and N 1s of WS-base as indicated in the figure.

Electrochemical characterization of WS-acid and WS-base for energy storage

The electrochemical properties of WS-acid, WS-base-derived ACs, and WS-control i.e., not activated sample were evaluated by cyclic voltammetry (CV) and galvanostatic charge-discharge (CD) techniques. The experiments were carried out in a 2 M NaOH solution using a standard three-electrode setup, as described in section 2.3. for supercapacitor applications. The CV and CD profiles are compared in Figure 5A–B. As observed, the CV curve of WS-acid is more quasi-rectangular, whereas that of WS-base is a little more like an elliptical shape. Nevertheless, both the curves feature no redox peaks, a typical feature of

electrochemical double-layer capacitors (EDLCs).^[37] Based on the preliminary studies, the WS-control sample is less electrochemically active, and activation enhances the capacitive nature. Among the samples studied, the current response from CV and the area under the curve from CV (Figure 5A) for WS-acid is comparatively higher than WS-base and WS-control, suggesting WS-acid is more electrochemically active than WS-base. It is further verified by CD (Figure 5B), tested under identical conditions, WS-acid takes a longer time to charge and discharge, therefore, capable of storing more charge. The near symmetrical shape of CD profiles is expected for EDLC carbon. A complete set of CV curves and CD profiles for WS-acid and WS-base is presented in Figure 6. The specific capacitance of

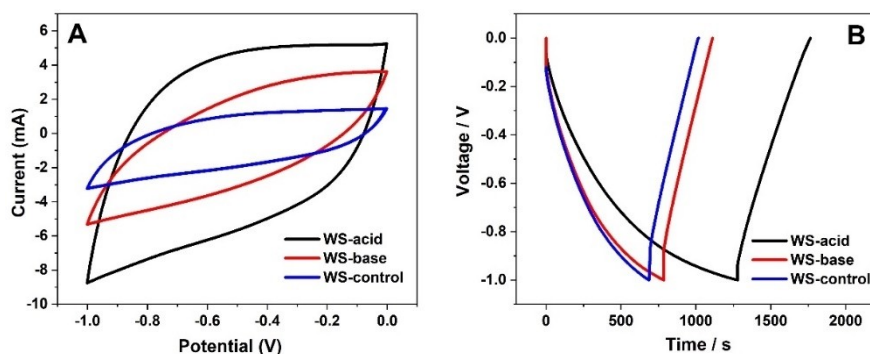


Figure 5. (A) Cyclic voltammograms (CV) of WS-acid, WS-base, and WS-control at a scan rate of 5 mV s^{-1} , and (B) galvanostatic charge-discharge (CD) profiles of WS-acid, WS-base, and WS-control at 2 mA cm^{-2} applied current density as labeled in the figure. The study is based on a three-electrode configuration with Hg/HgO as the reference electrode in a 2 M NaOH electrolyte.

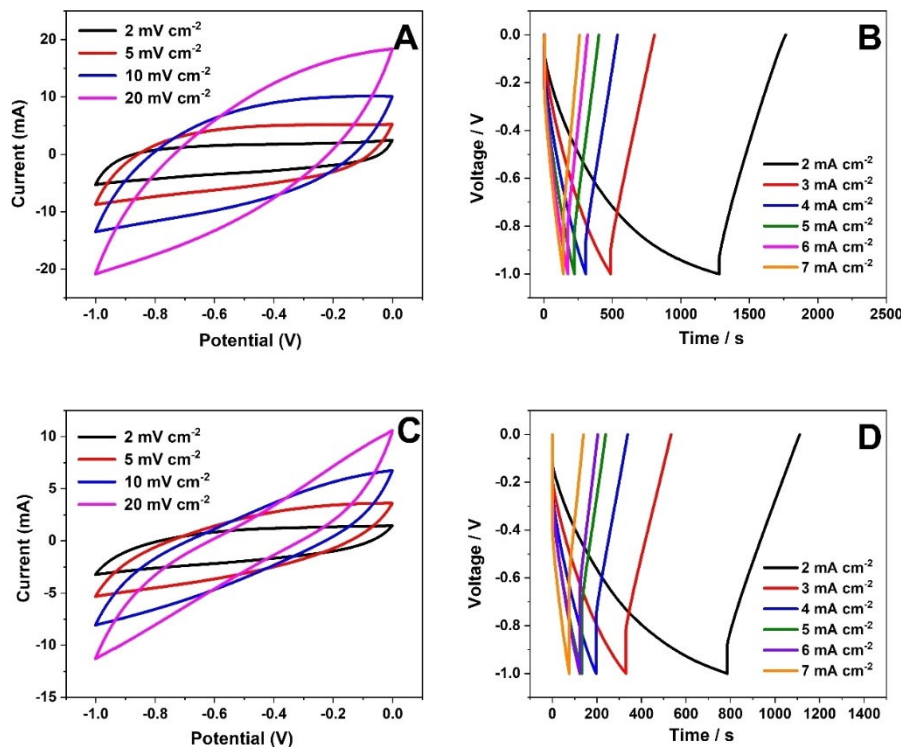


Figure 6. (A and B) Cyclic voltammograms (CV) at different scan rates and galvanostatic charge-discharge (CD) profiles at a different current density of WS-acid. (C and D) Cyclic voltammograms (CV) at different scan rates and galvanostatic charge-discharge (CD) profiles at a different current density of WS-base. The study is based on a three-electrode configuration with Hg/HgO as the reference electrode in a 2 M NaOH electrolyte.

WS-acid was calculated to be 162, 160, 151, 149, 142, 138 F g^{-1} at a current density of 2, 3, 4, 5, 6, and 7 mA cm^{-2} respectively. On the other hand, the calculated specific capacitance of WS-base was 106, 101, 94, 84, 81, and 75 F g^{-1} at a current density of 2, 3, 4, 5, 6, and 7 mA cm^{-2} respectively. The obtained values for WS-acid are substantially superior to that of WS-base. This may be directly attributed to the differences shown in their surface area, surface composition, and heteroatom with the surface functional groups. Therefore, WS-acid devotes lower diffusional limitations due to a hierarchical porous carbon network. For acid enabled sample, the surface functional groups such as $\text{C-SO}_3\text{-C}$ and S=C in the carbon framework promote the adsorption/desorption process that led to a larger quasi-rectangular capacitive curve.

To fabricate a device for practical applications, the best-performed WS-acid (negative electrode) has been paired up with (a) WS-acid to form an asymmetric device and (b) Zn-doped NiMoO_4 (ZNM as a positive electrode) to form an asymmetric device.

The CV and CD profiles of a symmetric device are shown in Figure 7A–C. The plots represent CV curves of the WS-base derived AC vs. WS-base derived AC at different scan rates, different potential windows, and the corresponding CD profiles at various current densities, respectively. The CV curve of the symmetric device displays a quasi-rectangular shape with no

redox (pseudocapacitive faradaic response) peaks, a typical characteristic of an electrochemical double-layer capacitor (EDLC). The CD profiles are observed to be a symmetric triangular shape, a typical capacitive material where reversible adsorption of ions occurs during the charging and discharging process. It is also seen from the respective CD profiles that IR drops are insignificant even for tested high current rates. Further, the CD curves also demonstrate a slope that is very close to linear. The specific capacitance of the symmetric device was calculated to be 56 F g^{-1} with a specific energy density of 8 Wh kg^{-1} at a high-power density of 480 W kg^{-1} at a current density of 2 mA cm^{-2} . At a higher current density of 7 mA cm^{-2} , the device was able to retain a specific capacitance of 26 F g^{-1} . Further, WS-acid was paired with ZNM and tested as an asymmetric device (Figure 7D to E). The fabrication of the symmetric device (ZNM vs. AC) is shown in Figure 7D with a safe extended potential window of 1.6 V. The extended potential window comes from the redox state of Ni in ZNM, which determined the energy density of the device. The CV curves at different scan rates are shown in Figure 7E with a minimal shift of redox potential, defining the process to be a reversible one. Based on the individual electrode performance, the potential window for the two-electrode system (WS-acid AC, 1.0 V vs. ZNM, 0.6 V) has been fixed at 1.6 V to avoid O_2 evolution reactions, as shown in Figure 7F. The asymmetric

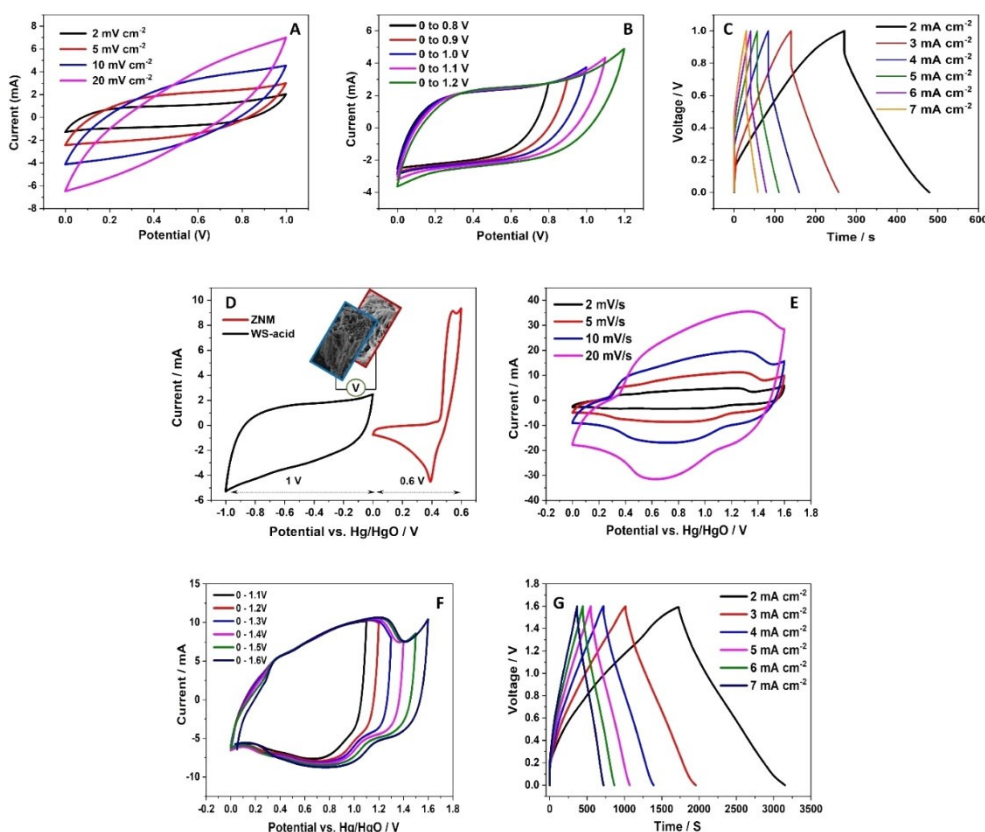


Figure 7. (A, B, and C) Cyclic voltammograms (CV) at different scan rates and potential windows; galvanostatic charge-discharge (CD) profiles at a different current density of symmetric (WS-acid) device. (D to G) Cyclic voltammogram (CV) of the individual electrode WS-base vs. ZNM in the negative and positive potentials; CVs at different scan rate and potential windows; and galvanostatic charge-discharge (CD) profiles at a different current density of asymmetric device – ZNM vs. WS-acid.

supercapacitor demonstrated an enhanced specific capacitance of 118 F g^{-1} with a high specific energy density of 42 Wh kg^{-1} at a high-power density of 382 W kg^{-1} when recorded at a current density of 2 mA cm^{-2} (Figure 7G). The increase in specific capacitance in this asymmetric device can be attributed to the contribution coming from the redox behavior of ZNM. The specific capacitance of ZNM vs. WS acid-derived AC (118 F g^{-1}) is comparable to the asymmetric device ZNM vs. commercial AC (122 F g^{-1}) as in our previous work.^[38]

Further insight on the charge transport behavior of the material was studied via electrochemical impedance spectroscopy (EIS) performed in a frequency range of 0.01 to 100 000 Hz at an open circuit potential as shown in Figure 8A–B for symmetric and asymmetric devices, respectively. The Figure 8 insets show the fitted equivalent circuit for both the device type. In both the plots, two distinct regions can be observed. The charge transfer resistance (R_{ct}) and solution resistance (R_s) are the semi-circle located in the high-frequency region and a Warburg impedance (W) which is linear in the low-frequency region. The values of R_s and R_{ct} before and after 1000 cycles are shown in the respective Figure inset for both symmetric and asymmetric devices. The value signifies that the device has a meagre resistance hence facilitating the charge transfer and even after 1000 long charge-discharge cycles, just a slight increase in the resistance values indicates that the material is suitable for long-term stability. To this end, another important aspect of the material, stability is investigated for a real-world application. The charge-discharge measurements were carried

out in a potential window of 1.0 V for symmetric and 1.6 V for asymmetric devices, respectively, at a current density of 5 mA cm^{-2} for 1000 continuous cycles. The discharge capacitance and its retention versus cycle number is shown in Figure 8C–D. At the end of the 1000 cycles, the symmetric device (Figure 8C) retained 97% of its initial capacitance, whereas the asymmetric device (Figure 8D) was able to hold 92% of its initial capacitance, which implied that both the devices were stable in a long-term operation. Both the symmetric and asymmetric devices demonstrated an excellent coulombic efficiency of 95% and 93%, respectively after being cycled for 1000 cycles. The FE-SEM image of the WS-acid electrode taken after being cycled for 1000 cycles (Figure S4) appears to retain its initial morphology without any visible fractures on the electrode surface.

Computational insights

Considering our experimental results, simulations are performed to study the structural and electronic properties of our samples as shown in Figure 9. Key information to perform the modeling is extracted from the XPS results (section 2.1). As observed from the XPS spectra, both the activation processes have led to the introduction of similar functional groups ($-\text{C}=\text{O}$, $-\text{C}-\text{OH}$, $-\text{C}-\text{C}-$, $\text{O}-\text{C}=\text{O}$, $\text{C}-\text{O}$, and N) except $\text{C}-\text{SO}_x-\text{C}$ and $\text{S}=\text{C}$ in WS-acid and K 2p as an intercalated product in WS-base. Hence, the presence of these functional groups, i.e., $\text{C}-\text{SO}_x-\text{C}$

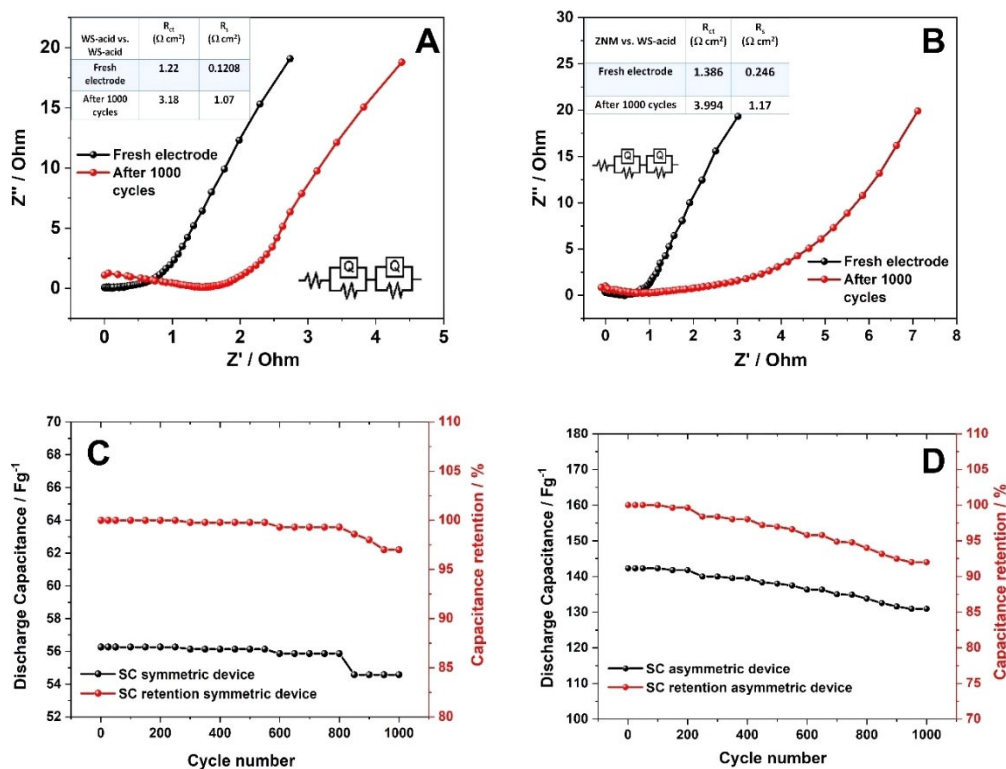


Figure 8. (A and B) Electrochemical impedance spectroscopy (EIS) results of symmetric and asymmetric devices for a fresh electrode and after 1000 cycles with the fitted circuit respectively as shown in the figure, and (C and D) Cycling stability of symmetric and asymmetric device at an applied current density of 5 mA cm^{-2} showing the devices capacitance and its retention (%).

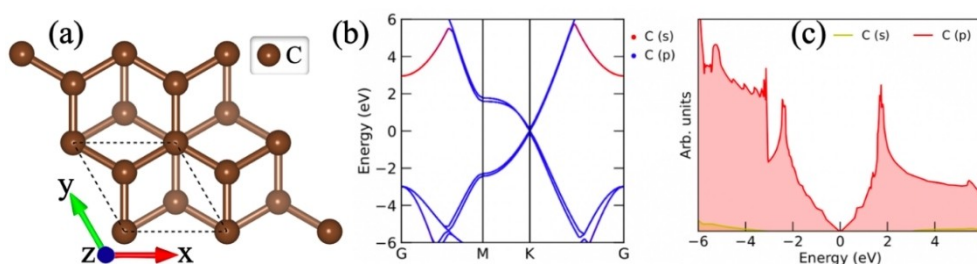


Figure 9. (a) Optimized structures of allotropes of carbon, (b) orbital contributed electronic band structure, and (c) projected density of states.

and S=C and K atom, are considered in the carbon structure and modeled to understand how it behaves.

The fully optimized structure of the pristine allotrope of carbon is presented in Figure 9a. The optimized lattice parameter is $a=b=2.466$ Å and $c=8.697$ Å, and the bond length between C–C is 1.424 Å which is consistent with previous literature.^[39] The electronic band structure along the high symmetric K-points G–M–K–G direction of the hexagonal Brillouin zone of a pristine allotrope of carbon was calculated as shown in Figure 9b. From the electronic band structure, C shows semi-metallic nature. It was seen that the C p-states is contributed near to the Fermi level in both valence band maximum (VBM) and conduction band minimum (CBM). The contribution of C s-states appears below the -3 eV in VBM and $+3$ eV in CBM. Similar electronic contributions are reflected in the projected density of states (PDOS), as shown in Figure 9c.

Further, the carrier mobility of electrons and holes of an allotrope of carbon was calculated to understand the electronic conductance based on deformation potential theory using the following equation:

$$\mu = \frac{eh^3 C_x}{k_B T m_x^* m_d E_x^2} \quad (1)$$

where, e , h , T and m^* represent the elementary charge, the Planck's constant, temperature, and effective mass, respectively. Here, m_d is calculated by $\sqrt{m_x^* m_y^*}$ and E_x represents the deformation potential, which is calculated by $\Delta V = E_x(\Delta a/a)$, where ΔV is the change of the band energy concerning the lattice dilation $\Delta a/a$ and C_x is the stretching modulus which is

calculated by the strain-energy curve. The calculated carrier mobility of electrons and holes and other related parameters using Equation (1) at temperature ($T=300$ K) for considered systems is summarized in Table 2. The carrier mobility of the hole is slightly larger than the electron mobility for pristine carbon (see Table 2).

Furthermore, the structural and electronic properties of allotropes of carbon are examined in the presence of the K atom which is present in the C framework as an intercalated product due to KOH activation. The optimized structure of allotropes of carbon in the presence of a K atom is presented in Figure 10a. It was seen that the optimized structure of allotropes of carbon-containing two-layer of carbon atoms is shifted to another orientation in the presence of the K atom. For the intercalation of K atoms, a $2 \times 2 \times 1$ supercell was taken. The optimized bond length between C–C atoms is 1.428 Å. Then, the projected electronic band structure and projected DOS was calculated to see the contribution of electronic states near to Fermi level, as shown in Figure 10b–c. The electronic band structure clearly shows that electronic orbitals of the K atom are strongly hybridized with C atomic orbitals. Therefore, the electronic states of K atoms appear near the Fermi level in the CBM, and the Fermi level is shifted towards the valence band side. Due to the shifted Fermi level towards the valence band side, the allotrope of carbon in the presence of the K atom display metallic nature. From PDOS, the large number of electronic states present at the Fermi level easily conduct the electrons from the valence band to the conduction band (see Figure 10c). The main contribution of the VBM is made by C p-states, while the CBM is formed by both C p-states and K s-states.

Table 2. Calculated electronic bandgap (E_g), the effective mass of electrons (e) and holes (h), deformation potential constants for electrons and holes ($E_{1(e/h)}$), elastic constants (C), and carrier mobilities of electrons ($\mu_{e/h}$) at temperature $T=300$ K.

System	E_g [eV]	$m_{(e/h)}^*$	$E_{1(e/h)}$ [eV]	C [J/m ²]	$\mu_{e/h}$ [10 ⁴ cm ² /Vs]
Pristine	0	0.192/0.19	4.42/3.18	712.66	2.64/2.77
C@K	0	–	–	–	–
C–SO _x –C and S=C					
x=4	0.33	0.238/0.271	10.44/10.34	898.49	1.75/1.38
x=3	0.19	0.179/0.195	14.65/6.44	816.04	1.43/6.24
x=2	0.14	0.169/0.253	10.63/8.01	869.02	3.24/2.55
x=1	0.28	0.645/0.267	9.81/8.50	770.15	0.23/1.80
x=0	0	–	–	–	–

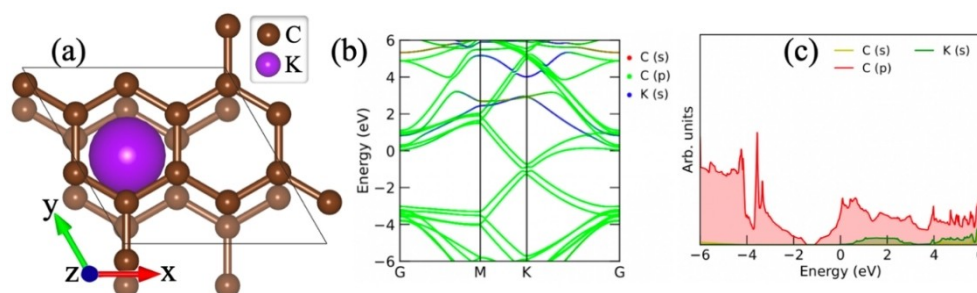


Figure 10. (a) Optimized structures, (b) orbital contributed electronic band structure, and (c) projected density of states of allotropes of carbon in the presence of K atom.

Finally, the structural and electronic properties of an allotrope of carbon in the presence of an S functional group in the form of $\text{C-SO}_x\text{-C}$ and S=C where $x=0, 1, 2, 3, 4$ as a result of acid activation, which is a highly active redox agent is investigated. The optimized structures of an allotrope of carbon in the presence of an S functional group in the form of $\text{C-SO}_x\text{-C}$ and S=C are presented in Figure 11a–e. Here, $2 \times 2 \times 1$ supercell was also used to see the interaction of the S functional group in the form of $\text{C-SO}_x\text{-C}$ and S=C . The optimized bond length between C-C/S-O/C-S are found to be $1.40\text{--}1.48/1.45/1.90 \text{ \AA}$, $1.40\text{--}1.46/1.47/1.81 \text{ \AA}$, $1.40\text{--}1.44/1.47/1.89 \text{ \AA}$, $1.40\text{--}1.44/1.50/1.89 \text{ \AA}$, $1.41\text{--}1.45\text{--}/1.88 \text{ \AA}$ for the S functional group in the form of $\text{C-SO}_x\text{-C}$ and S=C with $x=4, 3, 2, 1, 0$, respectively. The pristine allotrope of carbon has a C-C bond length of 1.424 \AA , which means that the S functional group in the form of $\text{C-SO}_x\text{-C}$ and S=C significantly interacts with the allotrope of carbon materials. Therefore, the top and bottom layers of carbon atoms are shifted towards the different orientations (see Figure 11). Due to the changes in structures, we have further calculated the electronic properties of an allotrope of carbon with an S functional group in the form of $\text{C-SO}_x\text{-C}$ and S=C (see Figure 12–13). From Figure 12, the electronic band structures of the S functional group in the form of $\text{C-SO}_x\text{-C}$ and S=C

carbon allotrope show semiconducting behaviour except when $x=0$.

In the presence of the S functional group in the form of $\text{C-SO}_x\text{-C}$ and S=C , the allotrope of carbon has strong hybridizations of orbitals of S and O atoms with C atoms therefore, it significantly opens the electronic bandgap in these systems. It was seen that the C p-states strongly contributed to the electronic states near the Fermi level, whereas p-states of O and S also have electronic states near the Fermi level, which is slightly lesser as compared to C p-states. The calculated electronic band gaps in the considered systems are $0.33, 0.19, 0.14, 0.28$ and 0.0 eV for $x=4, 3, 2, 1, 0$, respectively. From Figure 12e, the electronic states of C and S p-states are strongly hybridized, demonstrating a metallic nature. A finite number of electronic states are available to conduct the electrons from the valence band to the conduction band. The projected DOS shows similar electronic contributions of atomic orbitals (see Figure 13). The s-orbital has minimal contribution in each configuration. The carrier mobility of electrons and holes of the S functional group was calculated in the form of $\text{C-SO}_x\text{-C}$ and S=C in the allotrope of carbon, summarized in Table 2. It was seen that the carrier mobility of electrons in $\text{C-SO}_x\text{-C}$ and S=C functionalized carbon allotrope with $x=2$ is higher as compared to pristine carbon allotrope. It means that carrier mobility will be higher in $\text{C-SO}_x\text{-C}$ and S=C functionalized carbon allotrope as compared to the intercalated K atom in carbon allotrope. In summary, acid treatment improves the conductivity of the allotrope of carbon by introducing O_2 dopant along with other functional groups leading to increased hole density, decreasing the tunnel barriers at tube-to-tube interaction (as observed in FE-SEM image, section 2.1), and also the carrier delocalization is significantly increased which facilitates charge hopping.^[40] Our theoretical results, as well as hierarchical porous network morphology observed in the FE-SEM image, justify this reasoning very well. In addition to this, the presence of N atom in both WS-acid and WS-base shifts the Fermi level towards the valence band hence increasing the conductivity as demonstrated in previously reported literature.^[41]

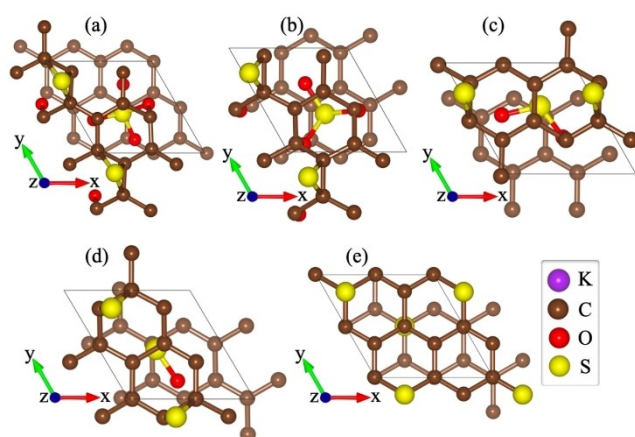


Figure 11. Optimized structures of allotropes of carbon in the presence of S functional group in the form of $\text{C-SO}_x\text{-C}$ and S=C where (a) $x=4$, (b) $x=3$, (c) $x=2$, (d) $x=1$, and (e) $x=0$.

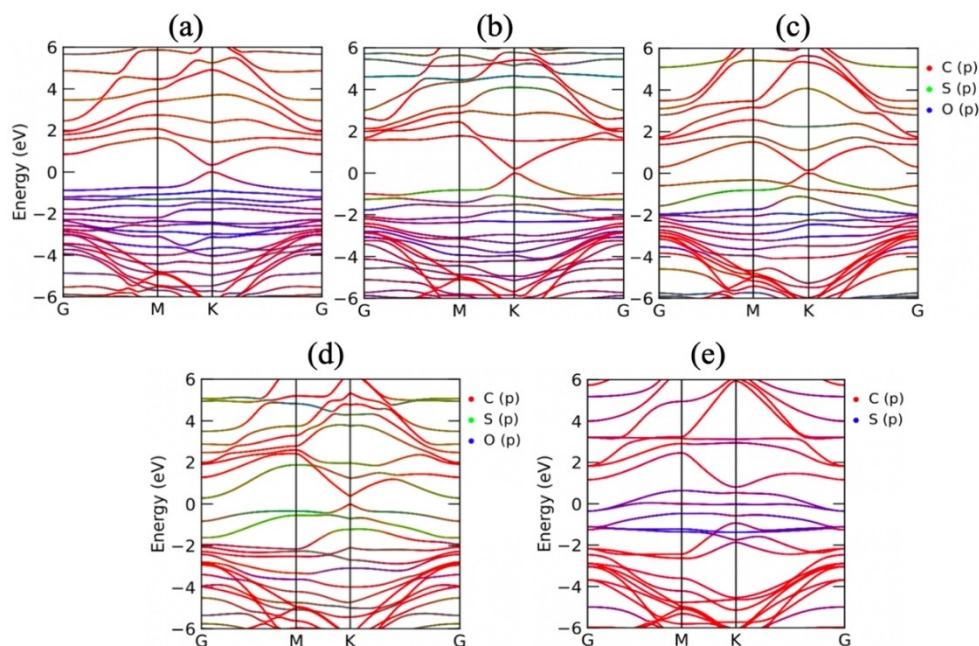


Figure 12. Orbital contributed electronic band structures of allotropes of carbon in the presence of S functional group in the form of $C-SO_x-C$ and $S=C$ where (a) $x=4$, (b) $x=3$, (c) $x=2$, (d) $x=1$, and (e) $x=0$.

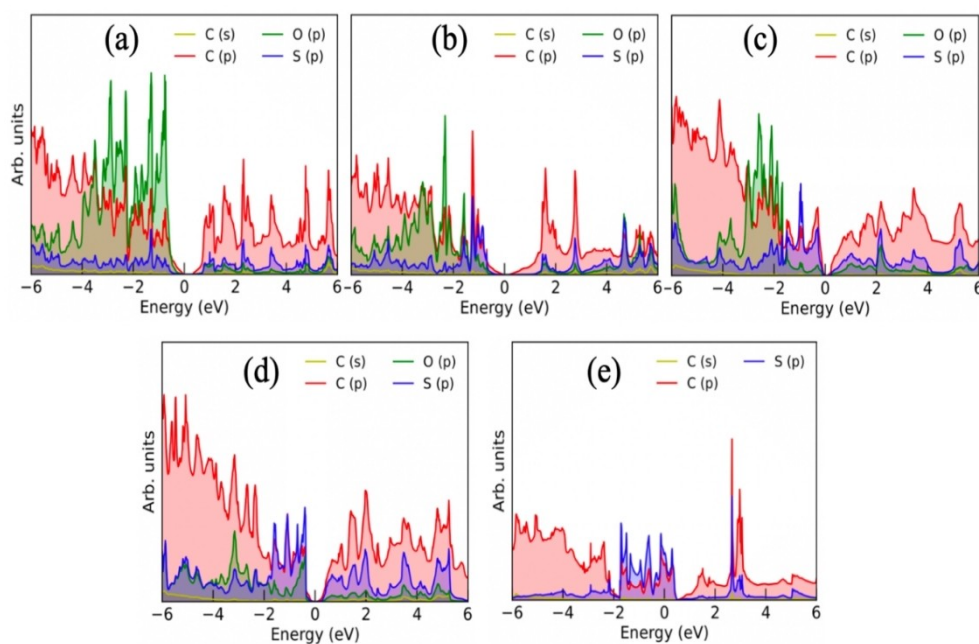


Figure 13. Projected density of states of allotropes of carbon in the presence of S functional group in the form of $C-SO_x-C$ and $S=C$ where (a) $x=4$, (b) $x=3$, (c) $x=2$, (d) $x=1$, and (e) $x=0$.

Conclusions

Activation-induced surface modulated activated carbon-derived from cereal straw is generated by changing the chemical activating agents by varying from acid to base reagents, which are found to be beneficial for controlling the carbon structure exhibiting enhanced capacitive properties. Herein, a hierarchical porous activated carbon is chemically activated in an electrolyte

containing either acid or base bringing insights on surface properties. We demonstrated excellent performance from a WS-acid derived AC from a symmetric (carbon-carbon) and asymmetric (carbon – ZNM) capacitors as a new carbon-based electrode material. The presence of $C-SO_x-C$ and $S=C$ functional groups in the acid-enabled material resulted in strong hybridization of S and O atoms with C atoms resulting in a reduced bandgap, hence increasing the electron/hole mobility.

The superior electrochemical performance of the WS-acid-derived AC can be explained by the surface modulation that enhanced the EDLC contribution. The Nyquist plot ascertains the diffusion of the electrolyte ions into the porous network of the carbon structure.

Experimental Details

Materials and synthesis

Wheat straw (WS) was obtained from Neridup, Esperance Wheatbelt, WA, Australia. Sulphuric acid, potassium hydroxide, and sodium hydroxide of analytical grade were procured from Sigma-Aldrich and used without further purification. The as-received wheat straw was washed with a copious amount of distilled water, dried well in the oven at 60 °C, pulverized, and then sieved using a sieve of diameter 70 μm . WS-powder was then carbonized at 800 °C under an N_2 atmosphere at the heating rate of 5 °C min^{-1} for 60 mins. 0.5 g of carbon thus obtained was then impregnated with conc. H_2SO_4 and KOH, weight ratio being maintained as 1:3 in both the cases. Thus, obtained activated carbon are labeled as "WS-acid" and "WS-base". These mixtures were well stirred using a magnetic stirrer for 2 h, the temperature is maintained at 60 °C. It was then completely dried in the oven maintained at 110 °C. Finally, it was activated at 800 °C for 2 h at a ramp rate of 5 °C min^{-1} under an N_2 atmosphere. Once the temperature is cooled down, the WS-acid sample is washed with 2 M NaOH, and WS-base is washed with 2 M HCl to neutralize it. Further, they are washed with a copious amount of distilled water till the filtrate pH is neutral. Later on, in an asymmetric device study, zinc-doped nickel molybdate (ZNM) is paired with WS-acid. The detailed preparation of ZNM can be found in our previous work.^[38] The various characterization methods used to study the synthesized material is detailed in Supporting Information.

Computational methods

The electronic structure calculations have been performed using density functional theory (DFT)^[42] as implemented in VASP software.^[43] The projected augmented wave (PAW) method^[44] in the form of generalized gradient approximations (GGA) using the Perdew-Burke-Ernzerhof (PBE) functional^[45] has been used to calculate the structural relaxations and self-consistent energy calculations. The kinetic energy cut-off is set to 500 eV for the plane-wave basis set, and Γ -centered K-points meshes of the Brillouin zone are set at $15 \times 15 \times 3$. The structural convergence criteria for the forces acting on the atoms and energy for the consecutive iterations are set at 10^{-3} eV/Å and 10^{-8} eV, respectively. The structures have been made using VESTA software.

Electrochemical characterization

To investigate the difference in electrochemical properties of the material based on the variation in synthesis procedure, electrochemical measurements were carried out in a 2 M NaOH solution using a BioLogic SP-150 workstation. For a three-electrode system, either WS-acid or WS-base served as a working electrode which was coated on a graphite sheet current collector; a platinum wire of 1 mm in diameter and 10 cm in length assisted as a counter electrode. Mercury-mercuric oxide (Hg/HgO) served as a reference electrode. The working electrode was fabricated by mixing WS-acid or WS-base (75 wt.%), carbon black (15 wt.%), and binder polyvinylidene fluoride (10 wt.%) well in an agate mortar along with 400 μL of N-methyl-2-pyrrolidone (NMP) to make a homogenous slurry. This coated graphite sheet (area of 1 cm^2) was then dried well in an oven maintained at 60 °C overnight. For the two-electrode configuration, both symmetric and asymmetric device was tested. Symmetric device was constructed using WS-acid-derived electrode both as a positive and negative, whereas an asymmetric device was constructed using WS-acid-derived as a negative electrode and ZNM as a positive electrode adopted from one of our previous works.²² The equations used for calculating specific capacitance (C_s), energy density (E), and power density (P) is detailed in Supporting Information.

Acknowledgements

Dr. Xiangpeng Gao and Ms. Saleha Quadsia both have been acknowledged for providing Wheat Straw samples. P.S. acknowledges the Murdoch University post-graduate scholarship and the facilities within the disciplines of Engineering and Energy, Chemistry, and Physics. P.S. acknowledges using the EM/XPS instrumentation at the John de Laeter Center, Curtin University. D.S. and R.A. thanks the Swedish Research Council (VR-2016-06014 & VR2020-04410) and J. Gust. Richert stiftelse, Sweden (2021-00665) for financial support. D.S. and R.A. gratefully acknowledge computational resources from the Swedish National Infrastructure for Computing SNIC and HPC2N. Open access publishing facilitated by Murdoch University, as part of the Wiley - Murdoch University agreement via the Council of Australian University Librarians.

Conflict of Interest

The authors declare no conflict of interest.

Data Availability Statement

The data that support the findings of this study are available in the supplementary material of this article.

Keywords: activated carbon • biowaste • density functional theory • supercapacitors • wheat straw

- [1] H. Garrett-Peltier, *Econ. Model* **2017**, *61*, 439–447.
- [2] J. Wang, P. Nie, B. Ding, S. Dong, X. Hao, H. Dou, X. Zhang, *J. Mater. Chem. A* **2017**, *5*, 2411–2428.
- [3] S. L. Candelaria, Y. Shao, W. Zhou, X. Li, J. Xiao, J. G. Zhang, Y. Wang, J. Liu, J. Li, G. Cao, *Nano Energy* **2012**, *1*, 195–220.
- [4] H. Terrones, R. Lv, M. Terrones, M. S. Dresselhaus, *Rep. Prog. Phys.* **2012**, *75*, 062501.
- [5] X. Zhang, T. Schiros, D. Nordlund, Y. C. Shin, J. Kong, M. Dresselhaus, T. Palacios, *Adv. Funct. Mater.* **2015**, *25*, 4163–4169.
- [6] D. W. Chang, H. J. Choi, A. Filer, J. B. Baek, *J. Mater. Chem. A* **2014**, *2*, 12136–12149.
- [7] H. Bi, X. He, H. Zhang, H. Li, N. Xiao, J. N. Qiu, *Renewable Energy* **2021**, *170*, 188–196.
- [8] W. H. Lee, J. H. Moon, *ACS Appl. Mater. Interfaces* **2014**, *6*, 13968–13976.
- [9] D. W. Wang, F. Li, L. C. Yin, X. Lu, Z. G. Chen, I. R. Gentle, G. Q. Lu, H. M. Cheng, *Chem. A Eur. J.* **2012**, *18*, 5345–5351.
- [10] D. W. Wang, F. Li, Z. G. Chen, G. Q. Lu, H. M. Cheng, *Chem. Mater.* **2008**, *20*, 7195–7200.
- [11] J. Gao, X. Wang, Y. Zhang, J. Liu, Q. Lu, M. Liu, *Electrochim. Acta* **2016**, *207*, 266–274.
- [12] C. Wang, S. H. Zhang, L. Zhang, R. Xi, D. P. Jiang, Z. Y. Chen, H. Huang, L. Y. Ding, G. B. Pan, *J. Power Sources* **2019**, *443*, 227183.
- [13] M. Masteri-Farahani, F. Ghorbani, N. Mosleh, *Spectrochim. Acta Part A* **2021**, *245*, 118892.
- [14] A. Zhao, J. She, C. Xiao, J. Xi, Y. Xu, D. Manoj, Y. Sun, F. Xiao, *Sens. Actuators B* **2021**, *335*, 129683.
- [15] B. Bayatsarmadi, Y. Zheng, A. Vasileff, S. Z. Qiao, *Small* **2017**, *13*, 1700191.
- [16] Q. Abbas, R. Raza, I. Shabbir, A. G. Olabi, *J. Sci. Adv. Mater. Devices* **2019**, *4*, 341–352.
- [17] Department of Primary Industries and Regional Development (2019), Western Australia. Available at <https://www.agric.wa.gov.au/grains-research-development/western-australian-wheat-industry>.
- [18] R. Kingwell, A. Abadi, *Biomass Bioenergy* **2014**, *61*, 58–65.
- [19] L. S. Pedersen, H. P. Nielsen, S. Kiil, L. A. Hansen, K. Dam-Johansen, F. Kildsig, J. Christensen, P. Jespersen, *Fuel* **1996**, *75*, 1584–1590.
- [20] T. Tufail, F. Saeed, M. Afzaal, H. B. U. Ain, S. A. Gilani, M. Hussain, F. M. Anjum, *Food Sci. Nutr.* **2021**, *9*, 2335–2344.
- [21] L. Björnsson, T. Prade, *Waste Biomass Valorization* **2021**, *12*, 5649–5663.
- [22] J. Wang, S. Kaskel, *J. Mater. Chem.* **2012**, *22*, 23710–23725.
- [23] J. Romanos, M. Beckner, T. Rash, L. Firlej, B. Kuchta, P. Yu, G. Suppes, C. Wexler, P. Pfeifer, *Nanotechnology* **2012**, *23*, 015401.
- [24] M. Sevilla, A. B. Fuertes, *Mater. Chem. Phys.* **2009**, *113*, 208–214.
- [25] L. Ding, Z. Wang, Y. Li, Y. Du, H. Liu, Y. Guo, *Mater. Lett.* **2012**, *74*, 111–114.
- [26] J. Liang, Y. Jiao, M. Jaroniec, S. Z. Qiao, *Angew. Chem. Int. Ed.* **2012**, *51*, 11496–11500; *Angew. Chem.* **2012**, *124*, 11664–11668.
- [27] H. Li, Y. Gong, C. Fu, H. Zhou, W. Yang, M. Guo, M. Li, Y. Kuang, *J. Mater. Chem. A* **2017**, *5*, 3875–3887.
- [28] W. Xiong, J. Peng, Y. Hu, *Microporous Mesoporous Mater.* **2010**, *133*, 54–58.
- [29] S. Chi, G. Yu, X. Zhang, Y. Zhang, C. Liu, Z. Li, B. Li, Q. Cui, *BioResources* **2019**, *14*, 4603–4622.
- [30] H. Mou, B. Li, P. Fardim, *Energy Fuels* **2014**, *28*, 4288–4293.
- [31] M. Demir, A. A. Farghaly, M. J. Decuir, M. M. Collinson, R. B. Gupta, *Mater. Chem. Phys.* **2018**, *216*, 508–516.
- [32] Z. Q. Li, C. J. Lu, Z. P. Xia, Y. Zhou, Z. Luo, *Carbon* **2007**, *45*, 1686–1695.
- [33] C. Chen, D. Yu, G. Zhao, B. Du, W. Tang, L. Sun, Y. Sun, F. Besenbacher, M. Yu, *Nano Energy* **2016**, *27*, 377–389.
- [34] X. Liu, C. Ma, J. Li, B. Zielinska, R. J. Kalenczuk, X. Chen, P. K. Chu, T. Tang, E. Mijowska, *J. Power Sources* **2019**, *412*, 1–9.
- [35] L. Zhang, L. Y. Tu, Y. Liang, Q. Chen, Z. S. Li, C. H. Li, Z. H. Wang, W. Li, *RSC Adv.* **2018**, *8*, 42280–42291.
- [36] M. Wahid, G. Parte, D. Phase, S. Ogale, *J. Mater. Chem. A* **2015**, *3*, 1208–1215.
- [37] M. A. Garakani, S. Bellani, V. Pellegrini, R. Oropesa-Nuñez, A. E. D. R. Castillo, S. Abouali, L. Najafi, B. Martín-García, A. Ansaldi, P. Bondavalli, C. Demirci, V. Romano, E. Mantero, L. Marasco, M. Prato, G. Bracciale, F. Bonaccorso, *Energy Storage Mater.* **2021**, *34*, 1–11.
- [38] P. Sharma, M. M. Sundaram, T. Watcharatharapong, D. Laird, H. Euchner, R. Ahuja, *ACS Appl. Mater. Interfaces* **2020**, *12*, 44815–44829.
- [39] T. P. Kaloni, S. Mukherjee, *Mod. Phys. Lett. B* **2011**, *25*, 1855–1866.
- [40] J. N. Tey, X. Ho, J. Wei, *Nanoscale Res. Lett.* **2012**, *7*, 548.
- [41] L. Lin, J. Li, Q. Yuan, Q. Li, J. Zhang, L. Sun, D. Rui, Z. Chen, K. Jia, M. Wang, Y. Zhang, M. H. Rummeli, N. Kang, H. Q. Xu, F. Ding, H. Peng, Z. Liu, *Sci. Adv.* **2019**, *5*, 8337.
- [42] W. Kohn, L. J. Sham, *Phys. Rev.* **1965**, *140*, A1133.
- [43] G. Kresse, J. Furthmüller, *Phys. Rev. B* **1996**, *54*, 11169.
- [44] P. E. Blöchl, *Phys. Rev. B* **1994**, *50*, 17953.
- [45] J. P. Perdew, K. Burke, M. Ernzerhof, *Phys. Rev. Lett.* **1996**, *77*, 3865.

Manuscript received: April 8, 2022
Revised manuscript received: May 9, 2022
Accepted manuscript online: May 10, 2022